ORIGINAL PAPER

Optimum Wear Resistance Achieved by Balancing Bulk Hardness and Work-Hardening: A Case Study in Austenitic Stainless Steels

Hengyi Zhang[1] · **Lingyu Wang**[1] · **Jun Hu**[1] · **Guodong Wang**[1] · **Wei Xu**[1]

Abstract

Wear, which exists in all industries and walks of life, causes tremendous economic losses and even major disasters. To prevent damage caused by wear, Archard's theory suggests the use of materials with higher hardness. However, such materials are minimally formable and difficult to manufacture. Recent studies have reported that strain hardening is another factor that significantly affects wear resistance. In this study, to investigate the relative potential of each of these factors and examine the balance between the hardness and work-hardening properties under various working conditions, we selected 321 austenitic stainless steel as a candidate material. Cold-rolling, which improves the base strength of the material, was used to develop strain-induced α'-martensite. Simultaneously, the strain-hardening capability of the material was decreased. The wear resistance and corresponding failure mechanisms were evaluated using the ball-on-disc test under various loading conditions. The results indicate that wear resistance depends on the bulk hardness and loading conditions used. A series of microstructural analyses revealed that the wear resistance is closely related to the base strength and hardening capability of the material. Therefore, this study establishes an optimum hardness–strain hardening balance and elucidates the design of low-hardness, high-wear-resistance materials for future applications.

Keywords Wear resistance · Initial α'-martensite · Bulk hardness · Work-hardening

1 Introduction

Previous wear-resistant steel designs focused on improving bulk hardness [1]. While the high flow stress of the structure limits the strain to the elastic regime as long as the contact stress does not exceed the elastic limit, high hardness prevents indentation to the contact surface by wear. However, such designs cannot adapt to abrasive deformation through crystallographic defects or phase transformation [2]. The high hardness and fragility of steel are attributed to limited active sliding systems. Recent studies [2, 3] on low hardness aimed to improve wear resistance based on the higher hardness of the tribo-layer [4]. The hardness of this layer increases with work-hardening, which significantly impacts the wear resistance of the material [5, 6]. The degree of work-hardening is closely related to the wear condition. Studying the relationships between the various combinations of bulk hardness and work-hardening properties and wear resistance is necessary. Studies on dry sliding wear behavior [7] indicate that normal load significantly affects the wear rate. The wear resistance of materials is related not only to their properties [8] but also to the test conditions.

There have been several studies [3, 5, 9–12] on the relationship between hardness and wear resistance. The wear resistance of pearlite steel depends on the hardness of the worn-out surface; the wear resistance improves as the hardness increases[13]. The classic Archard's equation [14] requires materials with higher hardness values, and the contribution of the work-hardening properties to the wear properties is not considered. Materials with high hardening rates have advantages in terms of resistance to wear [15]. However, the wear resistance of bainite with high bulk hardness is worse than that of pearlite with lower hardness [16].

Hadfield steel has excellent wear properties under high-impact wear conditions owing to its work-hardening properties [17]. An optimum biphasic ratio applies to the wear resistance of dual-phase steel [18, 19]. An optimum combination of hardness and plasticity (ferrite $+\alpha'$-martensite) leads to the best wear behavior [20]. A study reported that

✉ Wei Xu
  xuwei@ral.neu.edu.cn

1   State Key Laboratory of Rolling and Automation,
    Northeastern University, Shenyang 110819, China

carbide-free bainitic steels with similar hardness values and different hardening capacities, owing to the greater stability of the retained austenite, exhibited better wear resistance [5]. When the mechanical stability is high enough to delay the conversion from austenite to α′-martensite, the wear resistance is reduced [10]. Austenitic stainless steel has low strength but high plasticity and an excellent strain-hardening capacity owing to the martensitic transformation induced by the deformation of the metastable austenite [21–33].

The increase in bulk hardness is caused by an increase in the volume fraction of α′-martensite during cold-rolling (CR) deformation. The strain-induced martensitic transformation [5, 10, 12, 34, 35] prevents the deterioration of the substrate [36–38]. This occurs not only during the CR [12, 39–41] process but also on the tribo-layer [29]. The higher hardness (range of α′-martensite 0–38 vol.%) leads to the deterioration of wear resistance [12]. However, another study found the opposite conclusion (range of α′-martensite 4–22 vol.%) [11]. The range of variation in the initial quantity of α′-martensite produced by CR strain in these studies is too small to draw definitive conclusions. The work-hardening property can be considered one of the most significant factors affecting wear resistance. A study of carbide-free bainitic steels with similar hardness and different work-hardening properties found that higher austenite stability leads to better wear resistance. [5]. When the mechanical stability is sufficiently high to delay the conversion of austenite to martensite, the wear resistance is reduced.[10]. Three metallurgical structures (pearlite, martensite, and bainite) with radically different hardness were subjected to three-body abrasive wear tests with silica [3]. Because of its work-hardening property, only the bainite structure with the highest wear resistance was hardened on an abraded tribo-layer. There still exists disagreement about the relationship between hardness and work-hardening.

In this study, to examine the balance between the hardness and work-hardening properties under various working conditions, we used 321 stainless steel as the model material. We introduced α′-martensite through CR to improve its hardness and reduce its work-hardening properties. The wear resistance was determined using the ball-on-disc wear test under wear conditions of normal load 50 and 25 N. The worn-out surfaces and microstructures of the tribo-layer were observed through scanning electron microscopy. The scratch hardness was used to analyze the hardness of the worn-out surface. The microhardness along the depth away from the worn-out surface was used to establish the optimal depth of the tribo-layer. This study establishes an optimum hardness-strain-hardening balance, which will aid in designing low-hardness, high-wear-resistance materials for various applications.

2 Experimental Procedure

2.1 Test Materials and Sample Preparation

The starting material was a commercial AISI 321 austenitic stainless steel and its chemical composition was (in wt. %): C–0.022, Si–0.56, Mn–1.36, Ni–9, Cr–17.33, Cu–0.154, Mo–0.1, N–0.013, Ti–0.197, and Fe–71.264. Metastable austenitic stainless steels undergo deformation-induced transformation to the bcc martensitic structure during CR [22, 24, 33] to produce microstructures of different proportions of α′-martensite and austenite. A plate specimen with an initial thickness of 3.5 mm was cold-rolled to produce five samples with reduced thicknesses by up to 0%, 10%, 25%, 35%, and 55% at 298 K, (the equivalent strain (ε_r) ~ 0, 0.12, 0.33, 0.49 and 0.92, respectively). The equivalent strains on the CR specimens are expressed as follows:

$$\varepsilon_r = \frac{2}{\sqrt{3}} \ln \left({t_0}/{t} \right) \tag{1}$$

where t_0 and t represent the thicknesses of the plate specimens before and after CR, respectively. Following the CR, specimens were prepared under various conditions of metallography and phase analysis (10 × 10 mm), ASTM G99 testing (disc of 40 mm diameter), and tensile testing (sample geometry A25). The longitudinal dimension of the sample was oriented in the rolling direction through wire electric discharge machining to preserve the original microstructure of the samples.

2.2 Characterization of Microstructures

To apply the backscattered electron (BSE) and X-ray diffraction (XRD) techniques, all samples (10 × 12 mm) were polished following the standard metallographic procedure and electropolished (Electromet4) at 298 K and 20 V for 20 s. A mixture of 700 ml glacial acetic acid (CH_3COOH) and 100 ml perchloric acid ($HClO_4$) was used as the electropolishing solution.

The microstructures for five different thicknesses were characterized through backscattered-electron imaging BSE, (JEOL JXA 8530F) at 20 kV.

Quantitative estimation of the relative volume fraction of martensite and austenite was obtained from X-ray diffraction patterns (Bruker, D8 Discover) through ASTM E975-03 in the Bragg–Brentano geometry, focusing the monochromator on the secondary beam at a scanning rate of $0.03°s^{-1}$ in the 2θ range from 40° to 100°. The integrated total intensity of all diffraction peaks for each phase is proportional to the volumetric fraction of the phase. The integrated intensity from any single diffraction peak crystalline plane is also

proportional to the volume fraction of that phase. The integrated intensity 'I' of any diffraction peak from phase 'i' is:

$$I_i^{hkl} = KR_i^{hkl}V_i / 2\mu \tag{2}$$

w h e r e $\quad K = \left(\frac{I_0 A \lambda^3}{32\pi r}\right)\left[\left(\frac{\mu_0}{4\pi}\right)\frac{e^4}{m^2}\right] \quad$ a n d $\quad R_{hkl} = \left(\frac{1}{v^2}\right)$ $\left[|F|^2 p \left(\frac{1+\cos^2 2\theta}{\sin^2 \theta \cos\theta}\right)\right]\left(e^{-2M}\right)$. where I_i^{hkl}: integrated intensity for (hkl) plane of i-phase, i: γ and α', K: the instrument factor; R_i^{hkl}: material scattering factor that depends on θ, interplanar spacing of hkl, and the composition and crystal structure of the phase i, V_i: volume fraction of phase i, v: volume of unit cell, F_{hkl}: structure factor for reflecting plane (hkl), p: multiplicity factor, e^{-2M}: temperature factor, λ: the wavelength of incident X-ray beam, μ: linear absorption coefficient, A: cross sectional area of incident X-ray beam, I_0: intensity of the incident beam, r: radius of diffractometer circle, e,m: charge and mass of electron.

Therefore, for a steel containing fcc-austenite (γ) and bcc martensite (α'), Eq. (2) may be written as,

$$I_\gamma = \frac{KR_\gamma V_\gamma}{2\mu}, I_{\alpha'} = \frac{KR_{\alpha'}V_{x'}}{2\mu}$$

If martensite and austenite are the only two phases present in a steel, then:

$$V_{\alpha'} + V_\gamma = 1 \tag{3}$$

The diffraction patterns used for this analysis were the (200) and (220) reflections of the γ phase and the (200) and (211) reflections of the α' phase. The crystal structure of each phase is known and the lattice parameters can be calculated from the peak positions and Bragg reflection angles. The volume fraction of martensite ($V_{\alpha'}$) for the ratio of measured integrated intensities of martensite and austenite peak to R-value is:

$$V_{\alpha'} = \left[\left(\frac{1}{q}\sum_{i=1}^{q}\frac{I\alpha i}{R\alpha i}\right) / \left(\frac{1}{P}\sum_{i=1}^{p}I\alpha i/R\alpha i\right) + \left(\frac{1}{q}\sum_{j=1}^{q}I\gamma j/R\gamma j\right)\right] \tag{4}$$

Equation (4) enables simultaneous calculation of the volume fraction of austenite and α'-martensite in 321 stainless steel from a single XRD scan by measuring the integrated intensity of each reflecting plane of the respective phases and calculating the parameter R for each phase.

2.3 Measurement of Mechanical Properties

The tensile test (Shimadzu, AGS-X) was repeated three times for each condition. The dimensions of the gauge segment of the tensile test piece were 1.6 mm (width) and 25 mm (length) parallel to the rolling direction. The thickness of the tensile specimens was 3.5, 3.15, 2.62, 2.28, and 1.57 mm. The microhardness measurements were carried out using a Vickers indenter (KB3000BVRZ-SA) at a load of 10 N. Each experiment was repeated three times, and the results were averaged.

2.4 Tribological Test

The experiments were performed on a ball-on-disk tribometer (MFT5000, Rtec USA) at 298 K in air with a relative humidity of 30%. The ball-on-disk test was performed to produce and evaluate the two-body abrasive wear behavior of specimens containing various volume fractions of α'-martensite. To reduce the chemical and physical interactions between the surfaces, tungsten carbide (WC) balls of diameter 10 mm were used as the friction pair; the microhardness of the balls was 1400 HV, which was higher than that of the steel under examination. The size of the balls was adequate for providing a wear track that made it feasible to observe the wear mechanisms developed during testing. Before the wear test, the surface of the disc specimen was polished following the standard metallography preparation and cleaned using an ultrasonic cleaner. The roughness analysis of the initial surfaces was performed using a vertical scanning white-light interfering profilometer. The root mean square roughness of the initial surfaces was 0.21 μm. To generate measurable and accurate wear, dry sliding wear tests were carried out at constant loads of 50 and 25 N at a mean linear velocity of 0.314 m/s, which corresponds to initial maximum Hertzian contact pressures of 2.3 and 1.8 GPa, respectively. The radius of the circle of the wear trace was 12.5 mm, and the sliding distance was 2000 m.

To determine the wear volumes, the profiles of the worn-out surfaces were measured following each test using a vertical scanning white-light interfering profilometer (MFT5000, Rtec USA). The wear track width was determined using the profiles of the worn-out surfaces. The wear volume was determined using this width according to Eq. (5), provided in ASTM standard G99 – 17.

$$w_d = 2\pi R\left[r^2 \sin^{-1}\left(\frac{d}{2r}\right) - \frac{d}{4}\left(4r^2 - d^2\right)^{0.5}\right] \tag{5}$$

where w_d is the wear volume of the disk, R is the wear track radius (0.125 m), d is the wear track width and r is the radius of the ball. Each test was repeated three times to verify the results.

2.5 Microstructural Changes in the Tribo-Layer

The worn-out samples were cleaned ultrasonically using ethanol for 10 min to investigate the morphology of the worn-out surface. The worn-out surfaces were characterized using scanning electron microscopy (SEM).

The scratch hardness test [42] was used to investigate the relationship between the hardness of the worn-out surface

and the wear resistance caused by wear. A large diamond Rockwell indenter with a tip radius of 100 µm and a cone angle of 120° was employed for the test. The indenter was pressed onto the center of the worn-out surface under a constant force, which caused the test sample to rotate slowly and uniformly. The geometric dimensions of the scratches developed were analyzed using a vertical scanning white-light interfering profilometer, and the result of the scratch hardness test was determined as follows:

$$H_S = \frac{\text{load}}{\text{projected load bearing area}} \tag{6}$$

Significant changes are often seen in the microstructure under the surface layers, referred to as the transformed tribological area (TTZ), owing to severe plastic deformation. The microstructures of the cross-section of the surface layer were characterized using backscattered electron (BSE) at 20 kV to investigate the distance up to which severe deformation occurs under the surface.

A 10gf Vickers microhardness tester (FM-700) was used to measure the hardness of the cross-sectioned specimens at a long distance from the worn-out surfaces. This was done to estimate the depth of the tribo-layer caused on the subsurface by the wear tests. Thus, the thickness of the hardened layer was defined as the distance from the surface to the area in which the hardness value reaches that similar to the bulk material.

3 Results and Discussion

3.1 Initial Microstructures

The microstructures with various thickness reductions produced by CR are shown in Fig. 1. A large quantity of α′-martensite was obtained in the CR samples owing to the strain-induced α′-martensite transformation[23, 25, 28, 29, 33] in metastable austenitic stainless steel. The microstructure of the as-received specimen is mainly composed of randomly oriented, equiaxed austenite grains and a certain amount of α′-martensite. The CR formed parallel lamellar structures. With an increase in the reduction caused by the CR, the deformation and lamellar structure become more evident, and the deformed structures become more homogeneous.

It is difficult to use metallographic techniques to evaluate the α′-martensite volume fraction. The XRD patterns recorded for samples of 321 stainless steel before and after CR are presented as Fig. 2a. When $\varepsilon = 0$, the (111) γ reflection is strong and the (110) α′ reflection is so weak that the peak almost disappears. When ε is increased from 0 to 0.92, the intensities of the (110) α′ reflection increase and the ratio of the (110) α′ peak strength to that of (111) γ also increases. The integrated intensity (area of peak above background) for martensite peaks (200) and (211) and for austenite peaks (200) and (220) were determined. The measured integrated
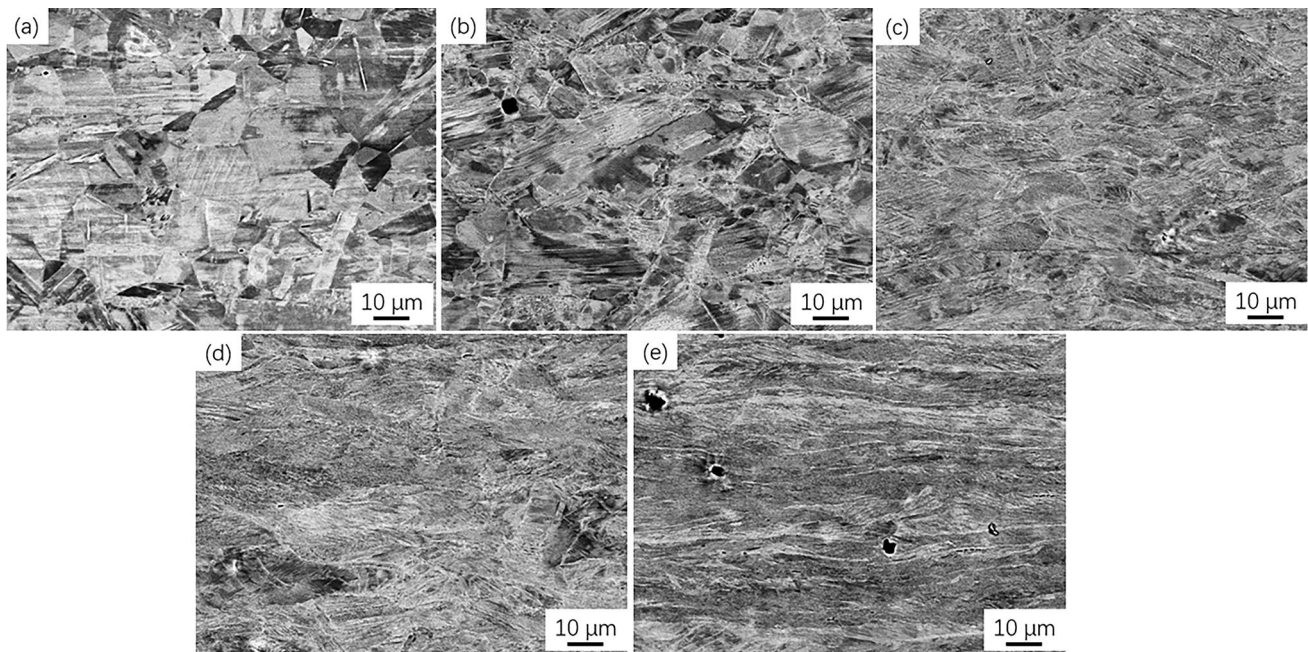

Fig. 1 SEM(BSE) micrographs captured after electrolytic polishing of **a** 2 vol.%, **b** 33 vol.%, **c** 55 vol.%, **d** 76 vol.%, and **e** 85 vol.% α′-martensite
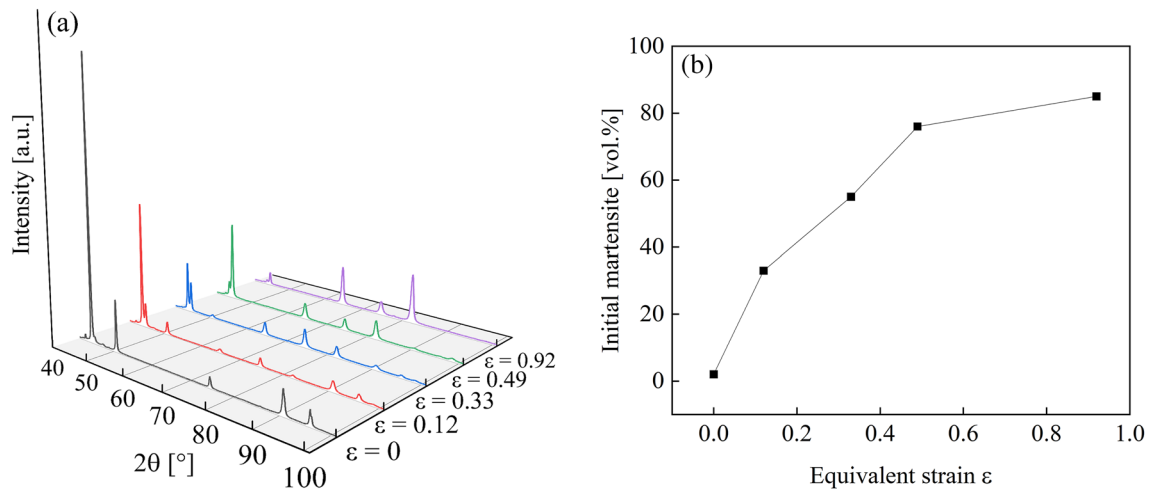
Fig. 2 The α'-martensite volume fraction of pre- and post- cold-rolling specimens: **a** X-ray diffraction patterns using Cu K$_\alpha$ radiation for the as-received and CR samples based on electrolytic polish, **b** change in α'-martensite volume fraction as a function of the equivalent strain

Table 1 R-value and the measured integrated intensity of martensite and austenite peaks

Peak	α' (200)	α' (211)	γ (200)	γ (220)
I (ε = 0)	106	818	87,957	21,566
I (ε = 0.12)	11,384	7386	30,347	21,766
I (ε = 0.33)	38,360	31,492	8089	52,579
I (ε = 0.49)	53,979	63,908	1002	35,553
I (ε = 0.92)	124,340	164,204	171	45,535
R	251.4	457.95	566.7	326.7

intensities and values of R for each peak are illustrated in Table 1.

Figure 2b depicts the variation in the volume fraction of α'-martensite as a function of equivalent strain. The as-received specimen consists primarily of an austenite phase (98 vol.%) and rarely an α'-martensite phase (2 vol.%).

The volume fraction of α'-martensite as a function of the equivalent strain increases monotonically, as reported previously[31, 32, 43]. With an increase in the rolling strain, the volume fraction of martensite is 33%, 55%, 76% and the maximum volume fraction of α'-martensite reaches 85 vol.% at ε ≈ 0.9. When the equivalent strain exceeds 0.33, the microstructures change from the main austenite phase to the main α'-martensite phase.

3.2 Mechanical Properties

The engineering stress–strain curves of various α'-martensite volume fractions are depicted in Fig. 3a. The yield strength (YS), ultimate tensile strength (UTS), elongation, and bulk hardness as functions of the initial α'-martensite volume fraction under all the conditions are depicted in Fig. 3b. 321-austenite stainless steel has a low YS of 340 MPa, UTS of 740 MPa, and large elongation of ~50%. An increase in
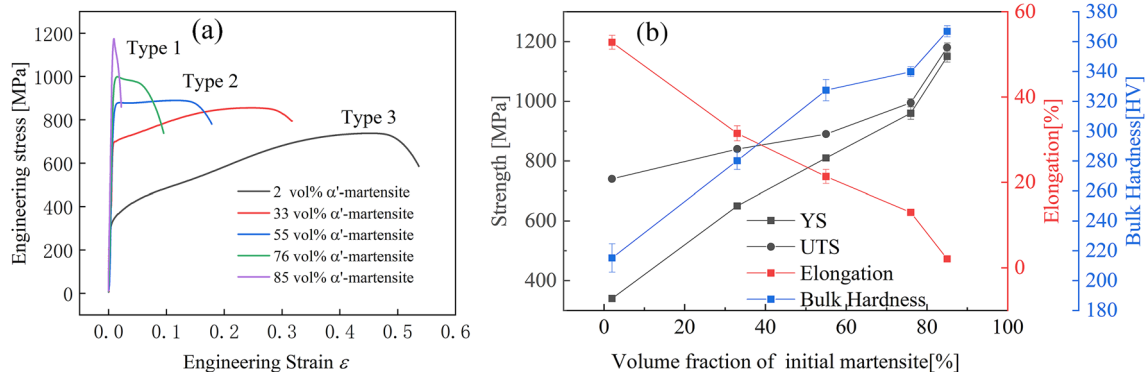

Fig. 3 Mechanical properties: **a** typical tensile curves and **b** YS, UTS, elongation and bulk hardness as functions of the α'-martensite volume fraction in the microstructures

the initial fraction of the α′-martensite volume increases the tensile strength and bulk hardness, whereas the elongation typically decreases. This indicates a monotonic increase in the hardness from 215 to 328 HV depending on the initial α′-martensite volume fraction.

The stress–strain curves are classified into three types, as depicted in Fig. 3a. The Type 1 curves represent 76 and 85 vol.% initial α′-martensite and indicate high susceptibility to sudden fracture owing to hard and brittle martensitic phases. The work-hardening property almost disappears, leading to the micro-fracturing of the surface layers during the wear. A limited amount of plastic strain and work-hardening is caused by wear, as depicted in Type 2 curves, which represent 33 and 55 vol.% initial α′-martensite. The results indicate that the α′-martensite represented by the Type 2 curves is able to withstand wear. The Type 3 curves represent 2 vol.% initial α′-martensite, which is soft and has high ductility. Although these materials exhibit high strains before fracture, these strains are generated at low stress levels. The low-level wear conditions create stresses that immediately cause the surface to shear beyond the critical strain, resulting in more material loss during wear. Therefore, the materials represented by Type 1 and 3 stress curves have no wear potential.

3.3 Tribological Properties

The volume loss under loads of 50 and 25 N is plotted in Fig. 4a as a function of the hardness. In the beginning, the volume loss of the steel decreases with increasing hardness. It then reaches a minimum and increases again with a further increase in hardness. The hardness of the sample corresponding to the best wear resistance is referred to as the optimum hardness. The results indicate that the relation between hardness and volume loss is V-shaped. The optimum hardness is 328 and 280 HV, corresponding to 55 and 33 vol.% of the initial α′-martensite tested at normal loads of 50 and 25 N, respectively. The minimum volume losses are 18.5 and 6.96 mm^3 at 55 and 33 vol.% of initial α′-martensite, respectively. These results indicate that the initial hardness cannot accurately predict wear behavior. Other properties such as the work-hardening capability of the material needs to be considered as well. Detailed discussions on the hardening capability characterization can be found later.

The pre-wear surface corresponds to the break-in stage, and the high wear rate cannot accurately reflect the wear resistance. The worn-out surface is the contact surface for the real workpiece. Consequently, scratches are used to characterize how the worn-out surface reacts to wear. The scratch hardness test was used to evaluate the hardness of the worn-out surface; the results are presented in Fig. 4b. With an increase in the initial α′-martensite volume fraction, the scratch hardness first increases and then decreases. The maximum value of scratch hardness corresponding to optimum wear resistance is identified for the 55 and 33 vol.% initial α′-martensite samples with normal loads of 50 and 25 N, respectively. For the same initial structure, increasing the normal load increases the hardness of the worn-out surface. Equation (7) indicates that the hardness of the worn-out surface is directly proportional to the normal load.

$$H \propto P(d/p)^2 \tag{7}$$

where H is the hardness of the worn-out surface, P is the normal load, d is the diameter of the friction pair, and p is the depth of penetration of the friction pair. The hardness of the worn-out surface under a normal load of 50 N is superior to that under a normal load of 25 N.
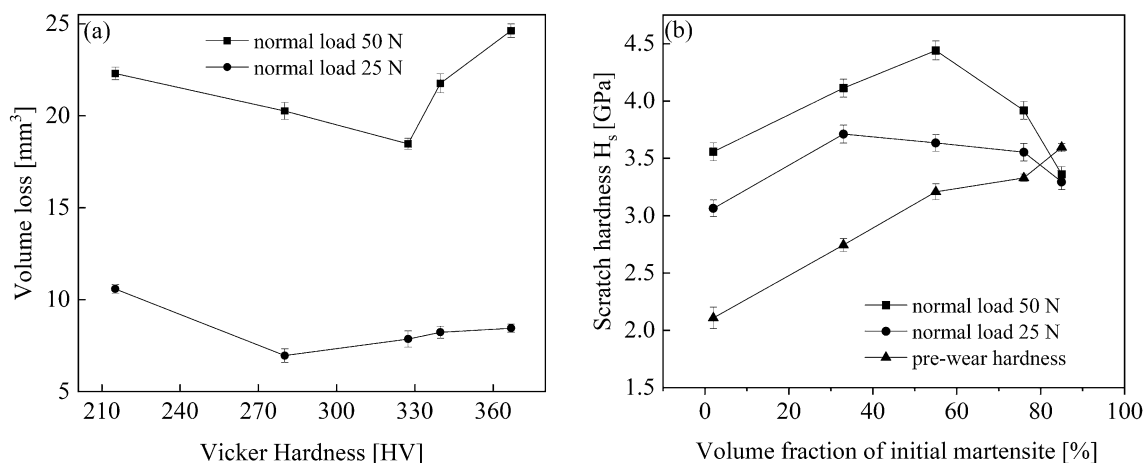

Fig. 4 Tribological properties: **a** volume loss as a function of bulk hardness and **b** scratch hardness of the pre- and post-wear surfaces

The major factor impacting the wear resistance is the hardness of the worn-out surface. In the case of 85 vol.% α′-martensite, the hardness of the worn-out surface is lower than the pre-wear surface hardness, and the wear causes softening. We conclude that the wear resistance of the 321 austenitic stainless steel is highly dependent on both the scratch resistance of the worn-out surface and the applied working conditions.

3.4 Morphological Characteristics of the Worn-Out Surface

Figure 5 presents representative SEM images of the morphology of the worn-out surfaces under various load conditions. A failure analysis was carried out to understand the main wear mechanism. As depicted in Fig. 5a, the wear track of the 2 vol.% initial α′-martensite under maximum wear conditions (F = 50 N) shows a large area of material detachment owing to softening of the alloy during the wear process. A large area of separation of the material indicates delamination, which is the main characteristic of adhesive wear. In Fig. 6a, owing to a high degree of deformation below the worn-out surface the adhesive wear is more significant, and surface cracks occur on the worn-out surface. The lower the degree of deformation beneath the worn-out surface, the lower the adhesive wear, as depicted in Fig. 5b–d. When the high shear deformation of the tribo-layer, it favors plastic deformation and delamination, and adhesive wear is the primary wear mechanism. As shown in Fig. 5f, under minimum wear conditions (F = 25 N), the worn-out surface of 55 vol.% initial α′-martensite displays a pitting pit, created as a crack propagates to the final fracture. The overall damage process occurs under small-scale plastic deformation, and macroscopically, the worn region appears free from plastic deformations. The main wear mechanism is contact fatigue. As depicted in Fig. 5e, the worn-out surface of 55 vol.% initial α′-martensite under the maximum wear conditions (F = 50 N) displays delamination and pits. Its wear mechanism is mostly adhesive wear mixed with a low amount of contact fatigue. Independently of the normal load, the tribo-layer disappears for the 76 and 85 vol.% α′-martensite samples. Owing to high brittleness, the subsequent formation and propagation of lateral cracks can lead to the formation of wear fragments through spallation. The material is primarily removed by micro-cutting. Therefore, abrasion wear is the primary wear mechanism for 76 and 85 vol.% initial α′-martensite, as indicated in Fig. 5g–j. The wear mechanism is closely related to the modification of the size of the tribo-layer.

3.5 Plastic Deformation of Deformed Tribo-Layer

The morphologies of the tribo-layer of the microstructures with 2–85 vol.% initial α′-martensite tested at normal loads of 50 and 25 N are presented in Figs. 6a–e and 7a–e, respectively. The morphologies of the tribo-layer and the matrix are different. Because the tribo-layer is hardened by wear, its hardness is higher than that of the matrix. The hardness of the cross-section relative to the depth of the surface is depicted in Fig. 8a and b for all the types of steel. When the initial α′-martensite is less than 55 and 33 vol.% under the wear conditions of the normal loads of 50 and 25 N, respectively, the wear is dominated by plasticity. The tribo-layer is extremely complex and heterogeneous; its grains close to the surface can be refined to the nanometer level (through mechanical milling).

Under a normal load of 50 N, the depth of the tribo-layer for 2, 33 and 55 vol.% initial α′-martensite is 120, 50 and 20 μm, respectively. Under a normal load of 25 N, the depth of the tribo-layer for 2 and 33 vol.% initial α′-martensite is 40 and 30 μm, respectively. The hardness close to the worn-out surface is higher than that of the matrix, and a clear work-hardening occurs. As the depth increases, the hardness and strain decrease. Under the contact Hertzian stress, plastic strains are imposed only on the top tribo-layer where the local stress exceeds the elastic limit. The plastic deformation is concentrated in the tribo-layer with a high strain gradient along the depth. A higher normal load leads to a higher contact Hertzian stress. For the same sample, the depth of the tribo-layer increases as the normal load increases. Under the contact Hertzian stress, the plastic strain can be initiated in the tribo-layer, where the local stress exceeds the elastic limit, and the elastic limit decreases with increasing depth. As the volume fraction of the initial α′-martensite increases and the work-hardening capacity decreases, the elastic limit increases, and the plastic strain gradient gradually decreases. The strain beneath the worn-out surface disappears when the local stress is lower than the elastic limit. The tribo-layer of 55 vol.% initial α′-martensite cannot be manufactured by wear under a normal load of 25 N. When the normal load increases to 50 N, F_{def} is large enough to deform below the worn-out surface of 55 vol.% initial α′-martensite. When the bulk hardness exceeds the optimum hardness, there is no tribo-layer beneath the worn-out surface, as depicted in Fig. 6d, e and 7 (c—e). The material is removed from the worn-out area only. The results indicate that there is no evident work-hardening beneath the worn-out surface. The depth of the tribo-layer depends on the wear conditions relative to the bulk hardness and work-hardening of the steels.

Fig. 5 SEM images of the worn-out surfaces of **a** 2 vol.%, **c** 33 vol.%, **e** 55 vol.%, **g** 76 vol.%, and **i** 85 vol.% initial α′-martensite at a normal load of 50 N and **b** 2 vol.%, **d** 33 vol.%, **f** 55 vol.%, **h** 76 vol.%, and **j** 85 vol.% initial α′-martensite at a normal load of 25 N
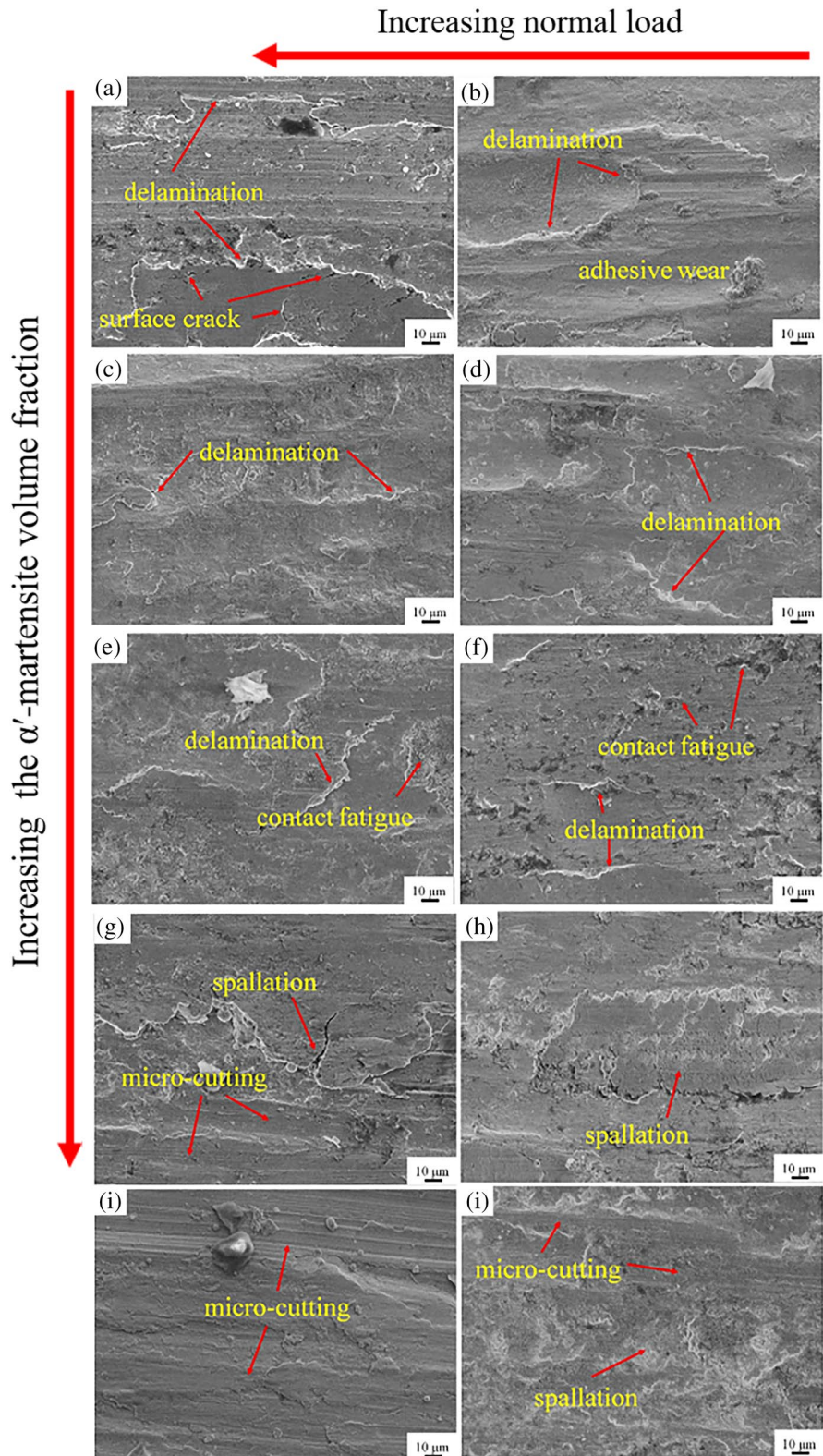
3.6 Work-Hardening of Tribo-Layer

When metals are subjected to a 'tribological challenge', their response depends on their pre-wear properties. Surfaces subjected to wear undergo extreme hardening, thereby increasing the hardness of the worn-out surface. The wear rate is the ratio of the volume loss to the normal load and wear distance. The wear resistance referred to in this study is
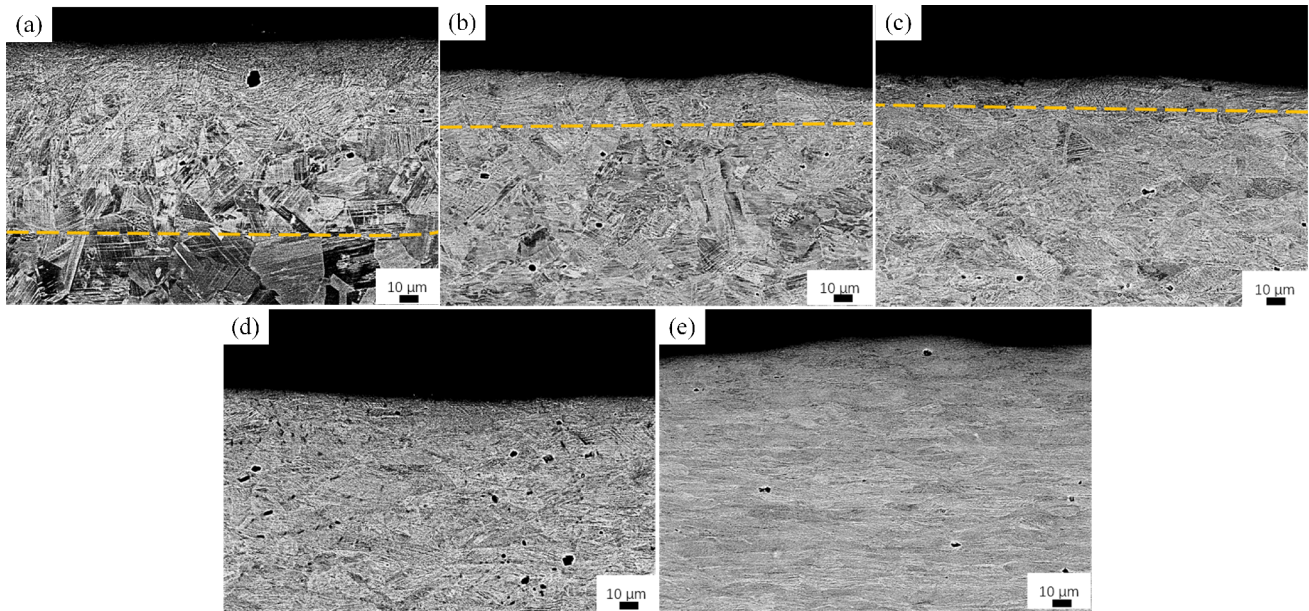
Fig. 6 Typical cross-section BSE micrographs of the tribo-layer under a normal load of 50 N for **a** 2 vol.%, **b** 33 vol%, **c** 55 vol.%, **d** 76 vol.%, and **e** 85 vol.% α′-martensite
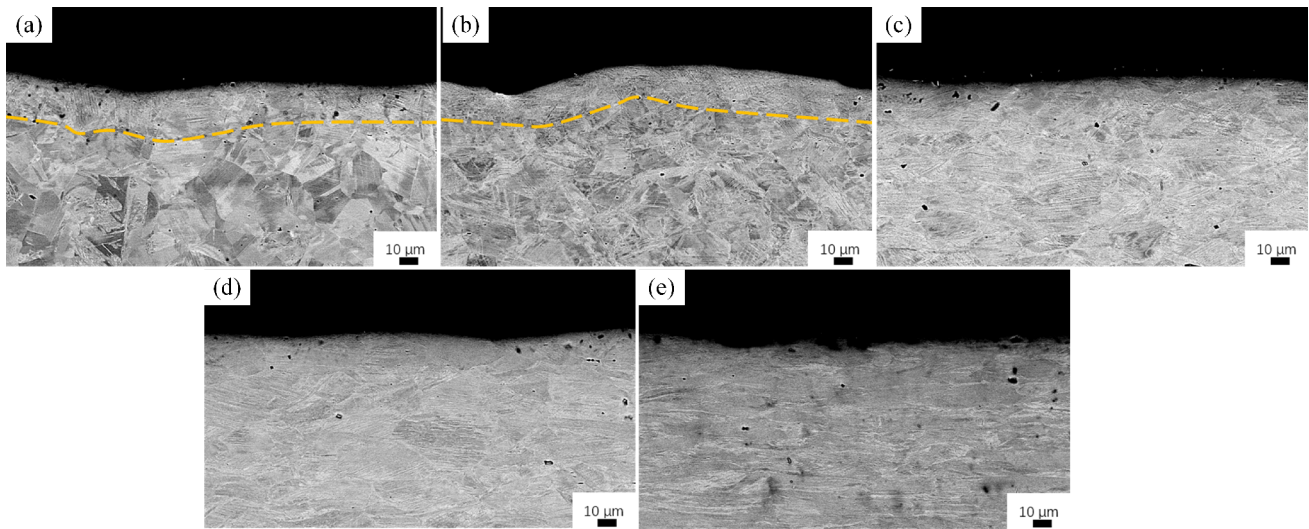

Fig.7 Typical cross-section BSE micrographs of the tribo-layer under a normal load of 25 N for **a** 2 vol.%, **b** 33 vol%, **c** 55 vol.%, **d** 76 vol.%, and **e** 85 vol.% α′-martensite

calculated using Eq. (8) given below, which is the reciprocal of the wear rate. Figure 9a presents the correlation of wear resistance with scratch hardness on the worn-out surface. It is evident that the wear resistance increases as the scratch hardness on the worn-out surface. There is a general tendency for wear resistance to increase as the hardness of the worn-out surface increases. However, a correlation between wear resistance and bulk hardness could not be detected. It can be inferred that the wear resistance is related to the bulk hardness and the scratch hardness on the worn-out surface,

which depends on the work-hardening properties and the normal load.

$$\text{wear resistance} = \frac{\text{normal load} \ \times \text{wear distance}}{\text{volume loss}} \quad (8)$$

In addition to bulk hardness, work-hardening behavior is also significant. The stress distribution in the tribo-layer varies depending on the differences in bulk hardness and work-hardening properties. This leads to various strain

Fig. 8 Hardness of the cross-section obtained in relation to the depth of the surface: **a** normal load of 50 N and **b** normal load of 25 N
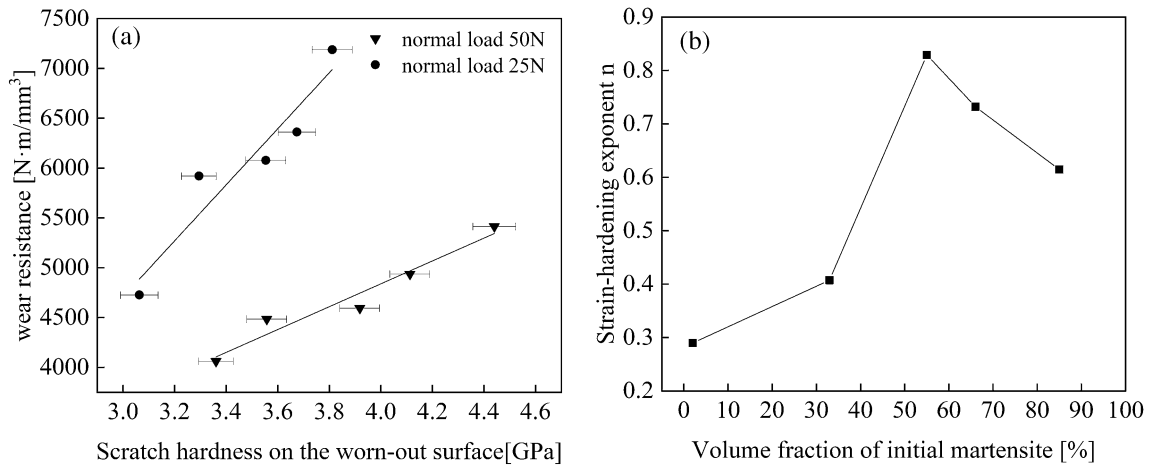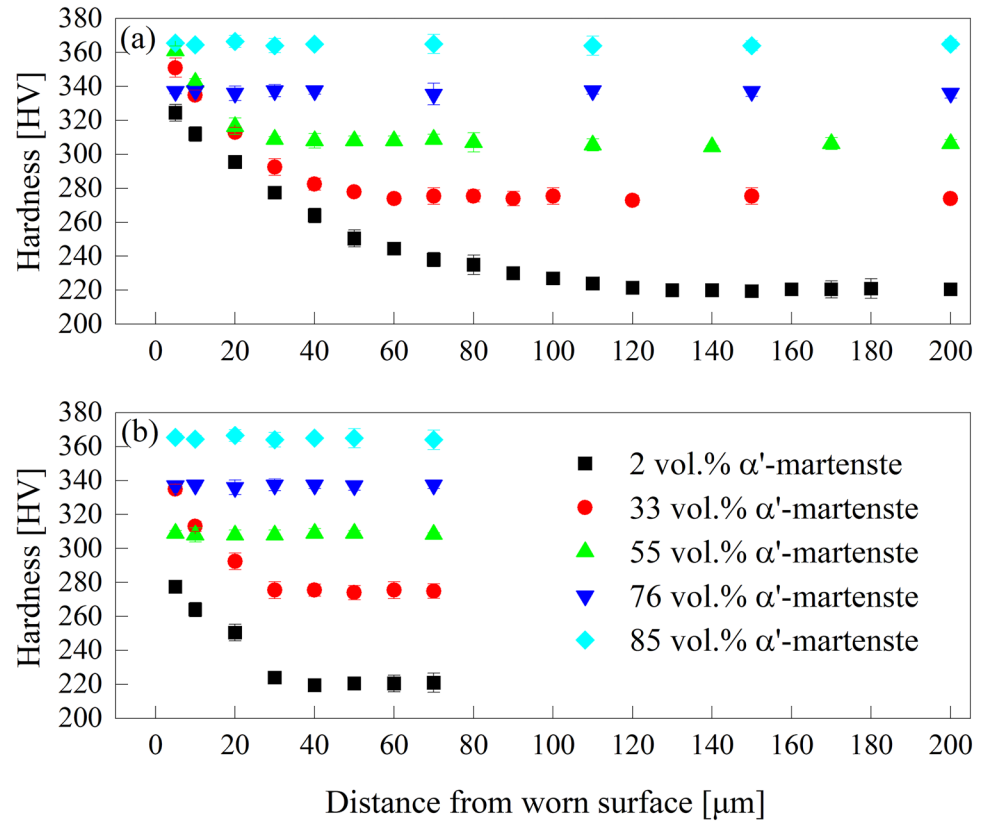

Fig. 9 Worn-out surface hardening caused by wear: **a** correlations of wear resistance with scratch hardness on the worn-out surface and **b** strain-hardening coefficient n as a function of the α′-martensite volume fraction

states in the friction transition zone, which leads to different worn-out surface hardnesses. The stress–strain curve in Fig. 3a indicates that as the volume fraction of the initial α′-martensite increases, the work-hardening rate decreases. Due to the severe plastic deformation in the tribo-layer caused by wear, we investigated the strain-hardening exponent n linked to the deformation properties. Figure 9b presents the strain-hardening exponent n as a function of the volume fraction of the initial α′-martensite. As the initial volume fraction of the α′-martensite increases, the value of n increases first and then decreases. The maximum value of n corresponds to 55 vol.% initial α′-martensite. This indicates that the material has a high uniform deformation ability and that the potential for local fracture is reduced. As the n value

increases, the local plastic deformation capacity of the material is improved, which is more conducive to improving wear resistance.

4 Conclusions

This paper presents the results of an experimental study on the dry sliding wear resistance in cold-rolled 321 austenitic stainless steel samples. The wear resistance was evaluated using the standard test method ASTM G99. The key findings of this study are summarized as follows:

1. The initially low wear resistance is attributed to the low bulk strength. The decrease in the wear resistance caused by the reduction of thickness owing to CR is attributed to the low hardening capability of the material and loss of material because of brittle fracture. The optimum wear resistance was achieved when the bulk hardness was high enough to resist the wear load, and a decent strain-hardening capability was still present to harden the material as wear proceeded. This study reports the existence of an optimum hardness–strain hardening balance. The optimum wear resistance was identified in 55 and 33 vol.% initial α'-martensite at normal loads of 50 and 25 N, respectively.
2. The scratch hardness can reflect the wear resistance of the worn-out surface. Wear resistance increased as the scratch hardness on the worn-out surface increased. The wear resistance is linked to the strain-hardening exponent n. As the n value increases, the local plastic deformation capacity of the material improves, which is more conducive to improved wear resistance. The scratch resistance of the 321 austenitic stainless steel was highly dependent on the work-hardening properties and the applied working conditions.
3. For 2 and 33 vol.% initial α'-martensite, the high shear deformation of the tribo-layer, which favored delamination, and adhesive wear was the primary wear mechanism. Under a normal load of 25 N, the worn-out surface of 55 vol.% initial α'-martensite displayed a pitting pit and the main wear mechanism was contact fatigue. For 55 vol.% initial α'-martensite, under a normal load of 50 N, the wear mechanism was mostly adhesive wear mixed with a low amount of contact fatigue. Owing to high hardness and brittleness, abrasion wear was the primary wear mechanism for 76 and 85 vol.% initial α'-martensite.

Declarations

References

1. Trevisiol, C., Jourani, A., Bouvier, S.: Effect of hardness, microstructure, normal load and abrasive size on friction and on wear behaviour of 35NCD16 steel. Wear **388–389**, 101–111 (2017). https://doi.org/10.1016/j.wear.2017.05.008
2. Das Bakshi, S., Sinha, D., Ghosh Chowdhury, S., Mahashabde, V.V.: Surface and sub-surface damage of 0.20 wt% C-martensite during three-body abrasion. Wear **394–395**, 217–227 (2018). https://doi.org/10.1016/j.wear.2017.07.004
3. Das Bakshi, S., Shipway, P.H., Bhadeshia, H.K.D.H.: Three-body abrasive wear of fine pearlite, nanostructured bainite and martensite. Wear **308**, 46–53 (2013). https://doi.org/10.1016/j.wear.2013.09.008
4. Tyfour, W.R., Beynon, J.H., Kapoor, A.: The steady state wear behaviour of pearlitic rail steel under dry rolling-sliding contact conditions. Wear **180**, 79–89 (1995). https://doi.org/10.1016/0043-1648(94)06533-0
5. Moghaddam, P.V., Hardell, J., Vuorinen, E., Prakash, B.: The role of retained austenite in dry rolling/sliding wear of nanostructured carbide-free bainitic steels. Wear **428–429**, 193–204 (2019). https://doi.org/10.1016/j.wear.2019.03.012
6. Tressia, G., Pereira, J.I., Penagos, J.J., Bortoleto, E., Sinatora, A.: Effect of in-service work hardening on the sliding wear resistance of a heavy haul rail in the gauge corner. Wear **482–483**, 203979 (2021). https://doi.org/10.1016/j.wear.2021.203979
7. Téllez-Villaseñor, M.A., León-Patiño, C.A., Aguilar-Reyes, E.A., Bedolla-Jacuinde, A.: Effect of load and sliding velocity on the wear behaviour of infiltrated TiC/Cu–Ni composites. Wear **484–485**, 203667 (2021). https://doi.org/10.1016/j.wear.2021.203667
8. Lim, S.C.: Recent developments in wear-mechanism maps. Tribol Int **31**, 87–97 (1998). https://doi.org/10.1016/s0301-679x(98)00011-5
9. Liu, B., Li, W., Lu, X., Jia, X., Jin, X.: An integrated model of impact-abrasive wear in bainitic steels containing retained austenite. Wear **440–441**, 203088 (2019). https://doi.org/10.1016/j.wear.2019.203088
10. Liu, B., Li, W., Lu, X., Jia, X., Jin, X.: The effect of retained austenite stability on impact-abrasion wear resistance in carbide-free bainitic steels. Wear **428–429**, 127–136 (2019). https://doi.org/10.1016/j.wear.2019.02.032
11. Qin, W., Li, J., Liu, Y., Yue, W., Wang, C., Mao, Q., et al.: Effect of rolling strain on the mechanical and tribological properties of 316 L stainless steel. J. Tribol. (2019). https://doi.org/10.1115/1.4041214
12. Fargas, G., Roa, J.J., Mateo, A.: Influence of pre-existing martensite on the wear resistance of metastable austenitic stainless steels. Wear **364–365**, 40–47 (2016). https://doi.org/10.1016/j.wear.2016.06.018
13. Ueda, M., Uchino, K., Kobayashi, A.: Effects of carbon content on wear property in pearlitic steels. Wear **253**, 107–113 (2002). https://doi.org/10.1016/s0043-1648(02)00089-3
14. Liu, R., Li, D.Y.: Modification of Archard's equation by taking account of elastic/pseudoelastic properties of materials. Wear **251**, 956–964 (2001). https://doi.org/10.1016/s0043-1648(01)00711-6

15. Lindroos, M., Valtonen, K., Kemppainen, A., Laukkanen, A., Holmberg, K., Kuokkala, V.-T.: Wear behavior and work hardening of high strength steels in high stress abrasion. Wear **322–323**, 32–40 (2015). https://doi.org/10.1016/j.wear.2014.10.018

16. Viáfara, C.C., Castro, M.I., Vélez, J.M., Toro, A.: Unlubricated sliding wear of pearlitic and bainitic steels. Wear **259**, 405–411 (2005). https://doi.org/10.1016/j.wear.2005.02.013

17. Zhang, G.-S., Xing, J.-D., Gao, Y.-M.: Impact wear resistance of WC/Hadfield steel composite and its interfacial characteristics. Wear **260**, 728–734 (2006). https://doi.org/10.1016/j.wear.2005.04.010

18. Shukla, N., Roy, H., Show, B.K.: Tribological behavior of a 0.33% C dual-phase steel with Pre I/C hardening and tempering treatment under abrasive wear condition. Tribol T **59**, 593–603 (2016). https://doi.org/10.1080/10402004.2015.1094841

19. Xu, X., van der Zwaag, S., Xu, W.: The effect of martensite volume fraction on the scratch and abrasion resistance of a ferrite–martensite dual phase steel. Wear **348–349**, 80–88 (2016). https://doi.org/10.1016/j.wear.2015.11.017

20. Jha, A.K., Prasad, B.K., Modi, O.P., Das, S., Yegneswaran, A.H.: Correlating microstructural features and mechanical properties with abrasion resistance of a high strength low alloy steel. Wear **254**, 120–128 (2003). https://doi.org/10.1016/s0043-1648(02)00309-5

21. Pöhl, F., Hardes, C., Theisen, W.: Deformation behavior and dominant abrasion micro mechanisms of tempering steel with varying carbon content under controlled scratch testing. Wear **422–423**, 212–222 (2019). https://doi.org/10.1016/j.wear.2019.01.073

22. Souza Filho, I.R., Sandim, M.J.R., Ponge, D., Sandim, H.R.Z., Raabe, D.: Strain hardening mechanisms during cold rolling of a high-Mn steel: Interplay between submicron defects and microtexture. Mater Sci Eng A **754**, 636–649 (2019). https://doi.org/10.1016/j.msea.2019.03.116

23. Shi, Y., Yuan, M., Li, Z., La, P.: Two-step rolling and annealing makes nanoscale 316L austenite stainless steel with high ductility. Mater. Sci. Eng. A **759**, 391–395 (2019). https://doi.org/10.1016/j.msea.2019.05.054

24. Kim, M.T., Park, T.M., Baik, K.-H., Choi, W.S., Han, J.: Effects of cold rolling reduction ratio on microstructures and tensile properties of intercritically annealed medium-Mn steels. Mater. Sci. Eng. A **752**, 43–54 (2019). https://doi.org/10.1016/j.msea.2019.02.091

25. He, Y., Zhang, J., Wang, Y., Wang, Y., Wang, T.: The expansion behavior caused by deformation-induced martensite to austenite transformation in heavily cold-rolled metastable austenitic stainless steel. Mater. Sci. Eng. A **739**, 343–347 (2019). https://doi.org/10.1016/j.msea.2018.10.075

26. He, W., Li, F., Zhang, H., Chen, H., Guo, H.: The influence of cold rolling deformation on tensile properties and microstructures of Mn18Cr18 N austenitic stainless steel. Mater. Sci. Eng. A (2019). https://doi.org/10.1016/j.msea.2019.138245

27. Benzing, J.T., da Silva, A.K., Morsdorf, L., Bentley, J., Ponge, D., Dutta, A., et al.: Multi-scale characterization of austenite reversion and martensite recovery in a cold-rolled medium-Mn steel. Acta Materialia **166**, 512–530 (2019). https://doi.org/10.1016/j.actamat.2019.01.003

28. Amininejad, A., Jamaati, R., Hosseinipour, S.J.: Achieving superior strength and high ductility in AISI 304 austenitic stainless steel via asymmetric cold rolling. Mater. Sci. Eng. A (2019). https://doi.org/10.1016/j.msea.2019.138433

29. Aletdinov, A., Mironov, S., Korznikova, G., Konkova, T., Zaripova, R., Myshlyaev, M., et al.: EBSD investigation of microstructure evolution during cryogenic rolling of type 321 metastable austenitic steel. Mater. Sci. Eng A **745**, 460–473 (2019). https://doi.org/10.1016/j.msea.2018.12.115

30. Shintani, T., Murata, Y.: Evaluation of the dislocation density and dislocation character in cold rolled Type 304 steel determined by profile analysis of X-ray diffraction. Acta Materialia **59**, 4314–4322 (2011). https://doi.org/10.1016/j.actamat.2011.03.055

31. Hedayati, A., Najafizadeh, A., Kermanpur, A., Forouzan, F.: The effect of cold rolling regime on microstructure and mechanical properties of AISI 304L stainless steel. J. Mater. Process. Technol. **210**, 1017–1022 (2010). https://doi.org/10.1016/j.jmatprotec.2010.02.010

32. De, A.K., Murdock, D.C., Mataya, M.C., Speer, J.G., Matlock, D.K.: Quantitative measurement of deformation-induced martensite in 304 stainless steel by X-ray diffraction. Scripta Materialia **50**, 1445–1449 (2004). https://doi.org/10.1016/j.scriptamat.2004.03.011

33. Takaki, S., Tomimura, K., Ueda, S.: Effect of Pre-cold-working on diffusional reversion of deformation induced martensite in metastable austenitic stainless steel. ISIJ Int. **34**, 522–527 (1994). https://doi.org/10.2355/isijinternational.34.522

34. Efremenko, V.G., Hesse, O., Friedrich, T., Kunert, M., Brykov, M.N., Shimizu, K., et al.: Two-body abrasion resistance of high-carbon high-silicon steel: metastable austenite vs nanostructured bainite. Wear **418–419**, 24–35 (2019). https://doi.org/10.1016/j.wear.2018.11.003

35. Yan, X., Hu, J., Yu, H., Wang, C., Xu, W.: Unraveling the significant role of retained austenite on the dry sliding wear behavior of medium manganese steel. Wear (2021). https://doi.org/10.1016/j.wear.2021.203745

36. Saada, F.B., Antar, Z., Elleuch, K., Ponthiaux, P., Gey, N.: The effect of nanocrystallized surface on the tribocorrosion behavior of 304L stainless steel. Wear **394–395**, 71–79 (2018). https://doi.org/10.1016/j.wear.2017.10.007

37. Li, G., Chen, J., Guan, D.: Friction and wear behaviors of nanocrystalline surface layer of medium carbon steel. Tribol. Int. **43**, 2216–2221 (2010). https://doi.org/10.1016/j.triboint.2010.07.004

38. Yan, W., Fang, L., Zheng, Z., Sun, K., Xu, Y.: Effect of surface nanocrystallization on abrasive wear properties in Hadfield steel. Tribol. Int. **42**, 634–641 (2009). https://doi.org/10.1016/j.triboint.2008.08.012

39. Zhang, F.C., Lei, T.Q.: A study of friction-induced martensitic transformation for austenitic manganese steel. Wear **212**, 195–198 (1997)

40. Li, C.X., Bell, T.: Sliding wear properties of active screen plasma nitrided 316 austenitic stainless steel. Wear **256**, 1144–1152 (2004). https://doi.org/10.1016/j.wear.2003.07.006

41. Zandrahimi, M., Bateni, M.R., Poladi, A., Szpunar, J.A.: The formation of martensite during wear of AISI 304 stainless steel. Wear **263**, 674–678 (2007). https://doi.org/10.1016/j.wear.2007.01.107

42. Williams, J.A.: Analytical models of scratch hardness. Tribol. Int. **29**, 675–694 (1996). https://doi.org/10.1016/0301-679x(96)00014-x

43. Talonen, J., Hänninen, H.: Formation of shear bands and strain-induced martensite during plastic deformation of metastable austenitic stainless steels. Acta Materialia **55**, 6108–6118 (2007). https://doi.org/10.1016/j.actamat.2007.07.015